

Spatial resolution characterization of differential phase contrast CT systems via modulation transfer function (MTF) measurements

This content has been downloaded from IOPscience. Please scroll down to see the full text.

2013 Phys. Med. Biol. 58 4119

(<http://iopscience.iop.org/0031-9155/58/12/4119>)

View [the table of contents for this issue](#), or go to the [journal homepage](#) for more

Download details:

IP Address: 85.181.71.215

This content was downloaded on 10/09/2015 at 22:45

Please note that [terms and conditions apply](#).

Spatial resolution characterization of differential phase contrast CT systems via modulation transfer function (MTF) measurements

Ke Li¹, Joseph Zambelli¹, Nicholas Bevins¹, Yongshuai Ge¹
and Guang-Hong Chen^{1,2}

¹ Department of Medical Physics, University of Wisconsin-Madison, 1111 Highland Avenue, Madison, WI 53705, USA

² Department of Radiology, University of Wisconsin-Madison, 600 Highland Avenue, Madison, WI 53792, USA

E-mail: gchen7@wisc.edu

Received 10 January 2013, in final form 1 May 2013

Published 17 May 2013

Online at stacks.iop.org/PMB/58/4119

Abstract

By adding a Talbot–Lau interferometer to a conventional x-ray absorption computed tomography (CT) imaging system, both differential phase contrast (DPC) signal and absorption contrast signal can be simultaneously measured from the same set of CT measurements. The imaging performance of such multi-contrast x-ray CT imaging systems can be characterized with standard metrics such as noise variance, noise power spectrum, contrast-to-noise ratio, modulation transfer function (MTF), and task-based detectability index. Among these metrics, the measurement of the MTF can be challenging in DPC-CT systems due to several confounding factors such as phase wrapping and the difficulty of using fine wires as probes. To address these technical challenges, this paper discusses a viable and reliable method to experimentally measure the MTF of DPC-CT. It has been found that the spatial resolution of DPC-CT is degraded, when compared to that of the corresponding absorption CT, due to the presence of a source grating G0 in the Talbot–Lau interferometer. An effective MTF was introduced and experimentally estimated to describe the impact of the Talbot–Lau interferometer on the system MTF.

(Some figures may appear in colour only in the online journal)

1. Introduction

In recent years, tremendous progress has been made in x-ray differential phase contrast (DPC) imaging (David *et al* 2002, Momose *et al* 2003, Pfeiffer *et al* 2006, 2008, Wen *et al* 2008, Olivo and Speller 2008, Kottler *et al* 2010, Kitchen *et al* 2011). Of the various DPC methods, one of the most promising techniques uses a grating-based Talbot–Lau interferometer and phase-stepping method to accurately measure the refraction angle of x-ray wavefronts (Momose *et al*

2003, Pfeiffer *et al* 2006). When extended to computed tomography (CT), the DPC imaging method can be used to simultaneously measure the internal distributions of an image object's linear x-ray attenuation coefficient, μ , and the decrement, δ , of the complex refractive index $n = 1 - \delta + i\beta$, with a single acquisition. The imaginary term, β , is proportional to the linear attenuation coefficient μ , which jointly depends on electron density (ρ_e), effective atomic number (Z), and the x-ray energy (E). In contrast, the real term, δ , only depends on electron density ρ_e and x-ray energy E . As a DPC-CT system can simultaneously provide DPC-CT and absorption CT (ACT) images, both ρ_e and Z of an image object can be quantitatively determined (Qi *et al* 2010). Note that simultaneous quantitative measurements of ρ_e and Z are offered only by the dual energy ACT imaging method in the current clinical practice. Therefore, the DPC-CT imaging method offers a novel alternative to quantitatively measure these two characteristics without invoking the dual energy x-ray ACT imaging method.

To evaluate the clinical potential of DPC-CT, the medical physics community has investigated extensively on the noise properties of DPC-CT, which are fundamentally different from those of ACT (Chen *et al* 2011, Raupach and Flohr 2011, Köhler *et al* 2011, Tang *et al* 2011, Zambelli *et al* 2011, Li *et al* 2013). However, the ultimate performance of the DPC-CT imaging system is jointly determined by the noise power spectrum, modulation transfer function (MTF), and specific imaging tasks (Li *et al* 2013), and few studies have been performed on the MTF of DPC-CT (especially experimental systems), despite its important role in determining the final detection performance and dose efficiency of a DPC-CT system.

The purpose of this paper is to systematically study the MTF of the DPC-CT imaging method using an experimental benchtop DPC-CT system. Since the major difference between a conventional ACT imaging system and a DPC-CT imaging system is the introduction of three x-ray gratings (i.e., the Talbot–Lau interferometer), the study focused on the influence of the Talbot–Lau interferometer over the system MTF. A new experimental method was developed to address several practical challenges in measuring the MTF of experimental DPC-CT systems, allowing the impact of the interferometer on the MTFs of both ACT and DPC-CT to be quantified.

2. Background: imaging physics model and a cascaded linear system model of DPC-CT

In an x-ray imaging system, x-ray photons undergo many different physical processes before they are measured by the detector. These processes may have different signal transfer characteristics at each spatial frequency component and thus may impact the final MTF of the system differently. In this section, we would like to provide a brief review of the physics model of the DPC imaging method as well as the linear cascaded system model used to analyze the MTFs of both DPC-CT and ACT in this work.

2.1. Imaging physics model

Enabled by a grating-based Talbot–Lau interferometer, a DPC-CT imaging system can be constructed using a low-brilliance diagnostic x-ray tube and a conventional x-ray detector (Pfeiffer *et al* 2006). Such a system allows one to acquire tomographic images of the local distribution of δ , which is related to the electron density, ρ_e , and x-ray energy, E , by

$$\delta = \frac{\rho_e r_0 h^2 c^2}{2\pi E^2}. \quad (1)$$

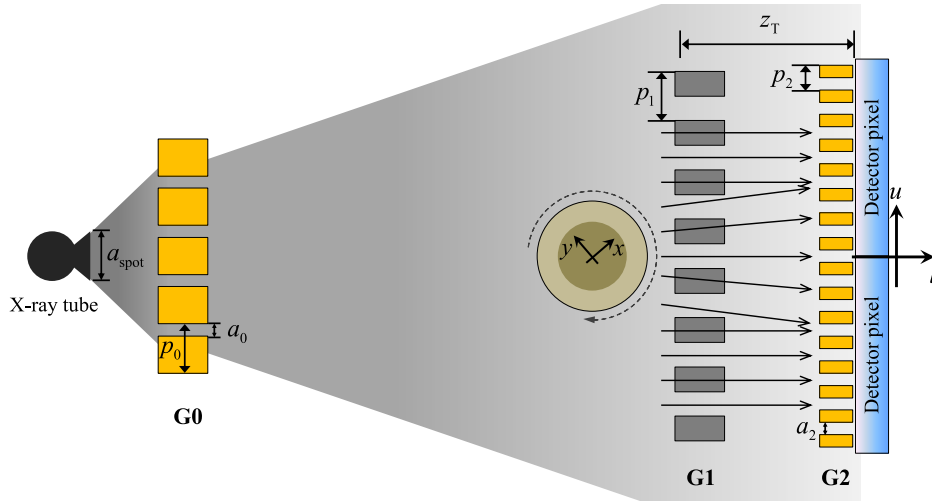


Figure 1. Illustration of a grating-based DPC-CT system. Spatially-coherent x-rays provided by a standard diagnostic x-ray tube and a source grating G0 can be used to generate an intensity modulation through a diffraction grating G1. Another G2 grating is placed in front of the detector to help analyze the phase shift of the diffraction pattern after an object is placed in the beam. DPC-CT images of the object can be reconstructed from multiple projections acquired at different view angles.

In equation (1), r_0 denotes the classical electron radius, c denotes the speed of light, and h denotes the Planck constant. Each projection data, $\phi(u)$, acquired from a DPC-CT system is related to the line integral of the first-order derivative of δ as follows:

$$\phi(u) = -\frac{2\pi z_T}{p_2} \frac{\partial}{\partial u} \int \delta(x, y) dl, \quad (2)$$

where the integral is performed along the direction of the x-ray projection, u is the horizontal axis of the detector plane, z_T is the distance between the G1 and the G2 gratings and is set to be equal to the fractional Talbot distance, and p_2 is the pitch of the G2 grating. A schematic illustration of the system is shown in figure 1. The same imaging system can simultaneously capture the conventional absorption-based projection signal $A(u)$ as well, which is related to the line integral of the linear attenuation coefficient μ by

$$A(u) = \int \mu(x, y) dl. \quad (3)$$

Using either a phase-stepping method (Momose *et al* 2003, Pfeiffer *et al* 2006) or a rotational moiré pattern analysis method (Bevins *et al* 2012), one can extract both the phase and absorption signals from the same set of intensity measurements. By acquiring multiple projections at different angular positions around the object being imaged, tomographic images of both DPC and absorption contrast can be reconstructed using the filtered backprojection algorithm. The only difference with respect to the reconstructions of the two CT images is that the ACT reconstruction uses the ramp filter kernel, while the DPC-CT reconstruction uses the Hilbert filter kernel (Huang *et al* 2006, Qi and Chen 2008).

2.2. Cascaded linear system model

A DPC-CT imaging system can be approximated to be linear and shift-invariant, as has been assumed and widely adopted for description of the ACT systems. Therefore, the signal transfer properties of DPC-CT can be analyzed using a cascaded linear system model, in which the final MTF can be considered to be the product of a series of signal transfer functions from different sub-stages. In the case of ACT, the MTF of can be formulated as

$$\text{MTF}_a(f) = T_{\text{spot}}\left(\frac{M-1}{M}f\right) \cdot T_{\text{det}}\left(\frac{f}{M}\right) \cdot T_{\text{win}}^a(f) \cdot T_{\text{intp}}(f), \quad (4)$$

where $f = \sqrt{f_x^2 + f_y^2}$ is the radial spatial frequency of the final reconstructed CT images, M is the geometric magnification factor of the image object, T_{spot} characterizes the geometric blurring due to the finite focal spot, T_{det} is the presampled MTF of the x-ray detector (Fujita *et al* 1992, Dobbins *et al* 1995), T_{win}^a corresponds to the window functions (e.g., Hann window) possibly used during the ACT reconstruction, and T_{intp} corresponds to the interpolation method. Discrete sampling stages, including detector sampling, tomographic angular sampling, and CT image sampling will not contribute to the final MTF aside from causing aliasing, therefore they are not included in the formulation of the MTF in (4).

A basic assumption of (4) is that the Talbot–Lau interferometer does not contribute to the MTF of ACT. The validity of this assumption will be experimentally studied in the paper. In comparison, the signal transfer performance of DPC-CT may be dependent on the Talbot–Lau interferometer. Therefore, the MTF of DPC-CT is formulated as

$$\text{MTF}_{\text{dpc}}(f) = T_{\text{spot}}\left(\frac{M-1}{M}f\right) \cdot T_{\text{TL}}(f) \cdot T_{\text{det}}\left(\frac{f}{M}\right) \cdot T_{\text{win}}^{\text{dpc}}(f) \cdot T_{\text{intp}}(f), \quad (5)$$

where T_{TL} characterizes the transfer function of the Talbot–Lau interferometer to input DPC signals. ACT and DPC-CT data acquired using the same hardware setup always have the same focal spot MTF T_{spot} and the detector MTF T_{det} , and the interpolation method T_{intp} is generally kept the same for ACT and DPC-CT reconstructions. If the window functions are set to be the same for ACT and DPC-CT (i.e., $T_{\text{win}}^a = T_{\text{win}}^{\text{dpc}}$), the difference between the MTFs of ACT and DPC-CT, if there is any, should be caused only by presence of the MTF of the Talbot–Lau interferometer $T_{\text{TL}}(f)$.

3. Experimental methods

3.1. Practical challenges in measuring the MTF of DPC-CT

A basic requirement for an accurate MTF measurement is that noise in the image of the MTF probe should be negligible compared with the signal, because the MTF describes the transfer properties of the signal instead of the noise. For ACT, this requirement can be easily met by scanning an MTF probe made of a highly x-ray attenuating material (e.g., tungsten). For DPC-CT, however, the dynamic range of ϕ is limited to $(-\pi, \pi)$, therefore the DPC signal from an object of extremely high phase contrast is subject to severe phase wrapping. For example, the DPC projection signal, ϕ , of a tungsten wire with radius R is

$$\phi(u) = \frac{2\pi z_T}{p_2} \frac{2\delta u}{[R^2 - u^2]^{1/2}}, \quad (6)$$

for $|u| < R$ and $\phi(u) = 0$ otherwise. At the mean x-ray energy of the experimental DPC-CT system used in this work ($E \approx 28$ keV), δ of tungsten is given by equation (2) is 4.12×10^{-6} .

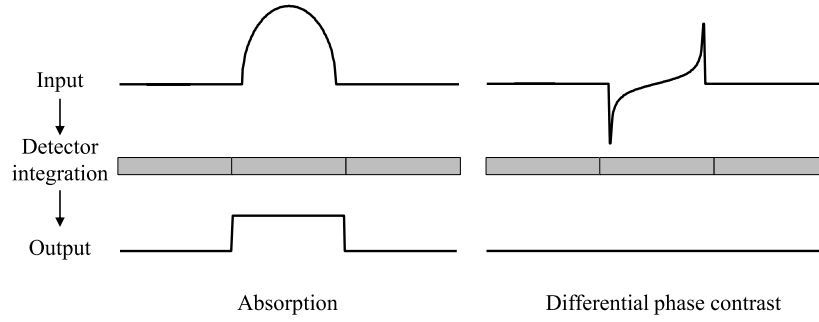


Figure 2. Unlike an absorption imaging system, a DPC imaging system is always insensitive to input signals measured by a single detector pixel.

By solving $\phi(x) = \pm\pi$, the thresholding coordinate u_t at which phase wrapping starts to occur is given by

$$u_t = \pm R \left[1 + \left(\frac{4z_T \delta}{p_2} \right)^2 \right]^{-1/2}. \quad (7)$$

For the system used in this work, $u_t = \pm 0.85R$. In other words, 15% (of the total length) of the DPC signal from the tungsten wire is out of the system dynamic range. Therefore, an object made with relatively low density should be used to measure the MTF of DPC-CT. Unfortunately, the signal-to-noise (SNR) ratio of the DPC-CT images of such an object is usually poor, as most experimental DPC-CT built so far have yet to be fully optimized.

Another practical challenge in measuring the MTF of DPC-CT is the difficulty of using fine objects: for ACT, it is an established protocol to measure the MTF using wires narrower than a detector pixel size to ease the correction for the finite wire width (Bischof and Ehrhardt 1977, Nickoloff and Riley 1985, Beutel *et al* 2000). The size correction is often performed by dividing the raw MTF, which is the Fourier transform of the object's profile, by the Fourier transform of the ground truth. For objects smaller than a detector pixel, this correction is no more than a few per cent (Bischof and Ehrhardt 1977). For large objects however, the size correction is challenging since its profile in the Fourier domain quickly drops to zero. On the other hand, the measurement of DPC-CT MTF has to use an object wider than a few pixels since the integration of any input DPC signal narrower than a detector pixel is zero (figure 2).

These challenges have been previously discussed in several numerical simulations (Köhler *et al* 2011 and Tang *et al* 2012). In these investigations, edges of cylindrical phantoms were used to measure the MTF of numerically modeled DPC-CT systems, which were assumed to have perfect x-ray temporal/spatial coherence and negligible image noise. For experimental DPC-CT systems, these assumptions in numerical simulations are no longer valid, preventing a straightforward generalization of MTF methods used in numerical simulations to experimental DPC-CT systems. In section 3.2, a new method that allows one to accurately determine the MTFs of experimental DPC-CT systems is reported.

3.2. Measurement of the MTF of DPC-CT

The MTFs of an experimental DPC-CT/ACT system were measured using a 0.3 mm graphite rod (0.3 mm B Pentel® super lead). The rod is made of graphite and a polymer binder and is widely available as a mechanical pencil refill. The δ value of the graphite rod measured at the mean operation x-ray energy of our system ($E \approx 28$ keV) is 3.89×10^{-7} . The rod was placed

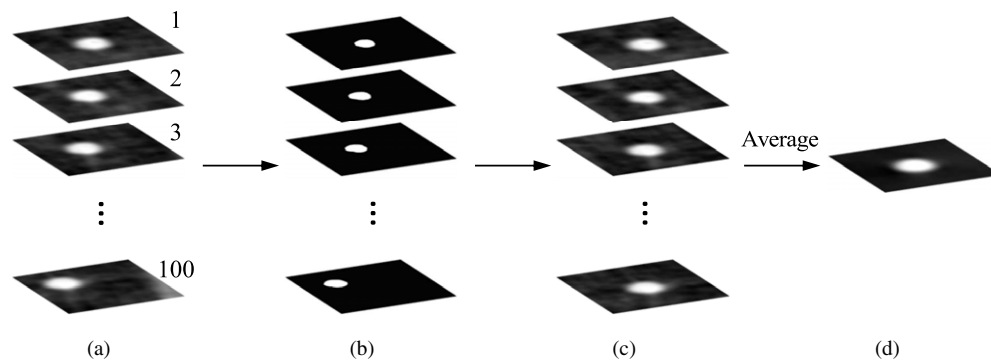


Figure 3. The slice-averaging scheme used in the MTF measurement. The incline of the object was exaggerated in (a); the actual measured angle between the pencil and the vertical axis is 1.20° . The images in (a) were thresholded to become binary images before the centroid of the graphite rod in each slice was determined. In (c), shifts were applied to move the centroid of each slice to the center of the displayed image. (d) is the high SNR image obtained by slice averaging.

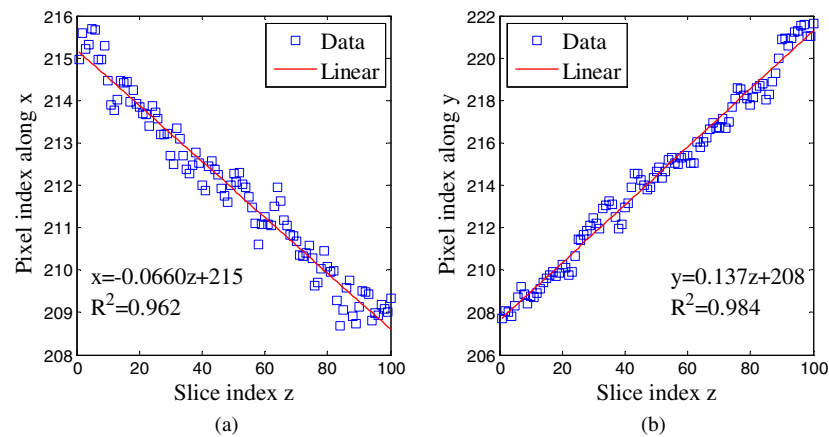


Figure 4. Measured x and y coordinates of the centroids of the 100 CT slices. Linear regression was used to perform the slice-by-slice registration.

upright in a water bath at the system isocenter, and less than 1% of its signal went beyond the dynamic range of the DPC-CT system.

Due to the relatively low phase and absorption contrast of graphite, slice averaging along the rotational axis of the CT system (z -axis) was carefully performed to boost SNR. The small angulation of the graphite rod was corrected using slice-by-slice registration (figure 3): the rod was modeled as a rigid and straight cylinder without twisting, thus the registration only considered the linear translation of the rod along the x - and y -axes. In each CT slice, the graphite rod was segmented from the surrounding water bath using MATLAB[®] functions *edge* and *imfill*. Each slice was then transformed to a binary image before the centroid of the rod in each slice was located. The measured x and y coordinates of the centroids were then plotted against the slice index z and linear regressions were performed to correct for errors induced by image noise (figure 4). In each MTF measurement, a stack of 100 neighboring slices were registered based on the measured centroid locations then averaged to a single

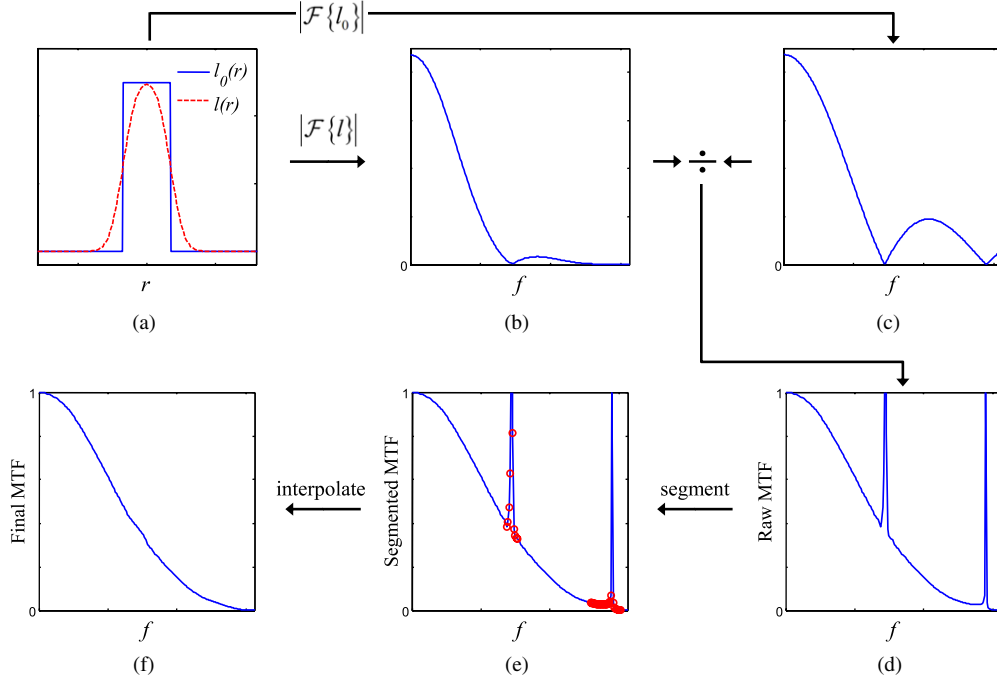


Figure 5. Flow chart for the first MTF measurement method. The Fourier transform of the measured radial profile of the object $l(r)$ was divided by the Fourier transform of the true object profile $l_0(r)$ to get the raw MTF in (d). Circles in (e) mark the segmented regions prone to the division-by-zero error, which were replaced by values interpolated from the neighboring region before the final MTF in (f) was generated.

image, the SNR of which is boosted to be ten times higher. Finally, a one-dimensional radial profile $l(r)$ through the center of the graphite rod was measured, where r denotes the radial distance to the rod center.

Since the measured profile of the rod, $l(r)$, is the true rod profile (l_0) blurred by the system MTF, the finite width of the graphite rod must be corrected in order to accurately determine the MTF. Two alternative methods were investigated in this work: the first method combines the conventional size-correction method with an interpolation scheme, in which the Fourier transform of the measured object profile $|\mathcal{F}\{l\}|$ is divided by the Fourier transform of the ground truth $|\mathcal{F}\{l_0\}|$. However, such an operation is subject to errors caused by division-by-zero, as $|\mathcal{F}\{l_0\}|$ drops to zero at nonzero multiples of $1/(2\pi R)$. Those errors can be corrected using an interpolation method, in which regions dominated by division-by-zero error can be segmented based on the derivative of $|\mathcal{F}\{l\}|$. Once those regions were identified, the errors were corrected by interpolation from neighboring values of the raw MTF. The process flow of this correction scheme is illustrated in figure 5.

The second method uses the edge response of the cylindrical phantom to measure the MTF, in which the first-order derivative (along the radial direction) of the edge of the true object profile was considered to be a Dirac delta function (Richard *et al* 2012, Tang *et al* 2012). Therefore, no size correction is needed by using this method, and the MTF is given by

$$\text{MTF}(f) = \left| \mathcal{F} \left\{ \frac{d}{dr} l(r) \right\} \right|. \quad (8)$$

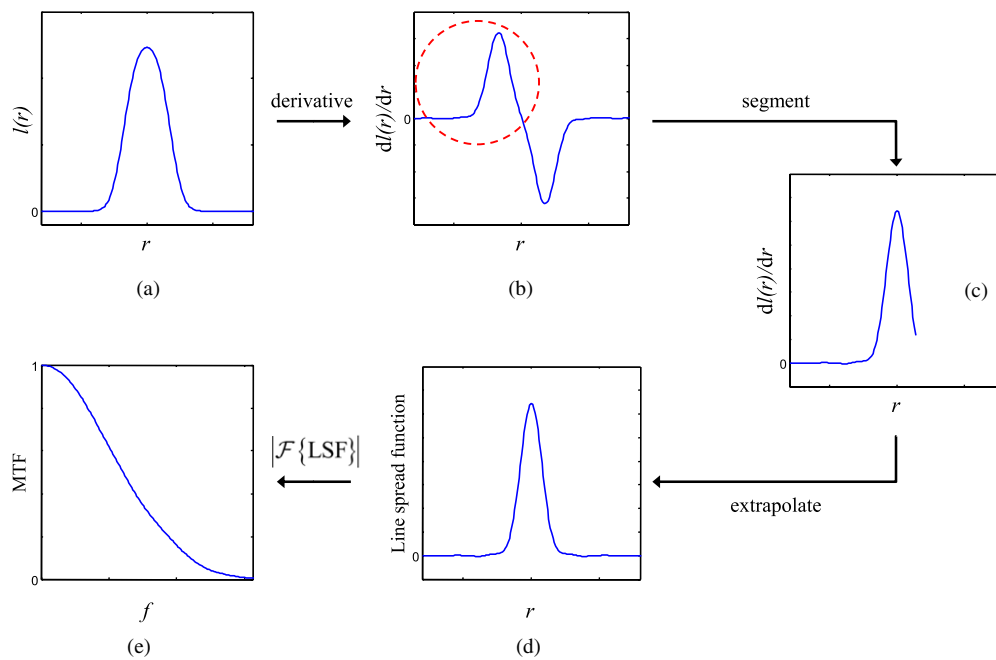


Figure 6. Flow chart for the second MTF measurement method. The first-order derivative of the measured object radial profile was calculated to get (b). Then the region corresponding to the edge of the cylindrical phantom (highlighted by the dashed circle) was segmented to obtain (c), which was extrapolated to get the complete line spread function (LSF) in (d). The final MTF in (e) was given by taking the magnitude of the Fourier transform of the LSF.

The work flow of the second method is summarized in figure 6. The results of our study show that there is no significant difference between MTFs processed using the two methods. In the remainder of this paper, the MTF results were calculated using the second method.

3.3. Measurement of the MTF of the ACT

The MTF of the ACT system (with all three gratings) was measured using the same phantom and method. To study the influence of the Talbot–Lau interferometer on the ACT MTF, four additional MTF experiments were performed under different grating setups: (1) the entire Talbot–Lau setup was removed; (2) the G0 and G2 gratings were kept in their designed positions while the G1 grating, which generates the Talbot diffraction pattern, was removed; (3) the G1 grating was removed while the G0 and G2 gratings were placed in the experimental system. The phase-stepping routine was disabled and the G0 and G2 gratings were rotated 90° with respect to the x-ray direction, so there were no in-plane periodic grating structures; (4) all three gratings were removed, and a 3.1 mm-thick aluminum (Al) plate was placed close to the tube to pre-filter the beam. Those four measurements allow a cascaded analysis of an potential influence of the gratings on the MTF of the ACT system.

3.4. Data acquisition and data analysis

MTFs of an experimental benchtop DPC-CT/ACT imaging system constructed in-house (Zambelli *et al* 2010) were measured. The system uses a rotating-anode diagnostic x-ray tube

(Varian G1582, Palo Alto, CA) with 0.1 mm nominal focal spot and a digital flat panel detector (Rad-icon Shad-o-Box 2048, Sunnyvale, CA) with $48\ \mu\text{m}$ pixel size. The magnification factor of the system is 1.2. The core components of the Talbot–Lau interferometer includes a source grating G0, a phase grating G1, and an analyzer grating G2. A detailed description of the system setup can be found in an earlier publication (Zambelli *et al* 2010).

Each CT scan of the MTF phantom took 720 projections at a 0.5° angular interval. The x-ray tube was operated at 40 kVp and 20 mA. At each angular position, the total exposure time was 40 s, divided over 8 phase steps. Both absorption and DPC projection images were extracted from the raw projection data. The FDK algorithm with bilinear interpolation was used to reconstruct 100 axial CT images of each contrast. Depending on the contrast mechanism, either a ramp filter (ACT) or Hilbert filter (DPC-CT) was used during the reconstruction. No apodization filter was applied. The reconstruction field-of-view (FOV) and matrix size was 4 mm and 400×400 , respectively. All MTF measurements were repeated in five distinct regions along the z -axis of the rod to generate the corresponding 95% confidence interval (± 2 times the standard error).

In order to mitigate signal aliasing that may affect the accuracy of the MTF measurement, the reconstruction sampling rate is kept to be four times higher than the detector sampling rate. In addition, the angular sampling rate of the CT acquisition ($\Delta\theta = 0.5^\circ$) is more than two times higher than the required angular sampling rate, which is determined by the reconstruction FOV and the detector sampling distance Δu as $\Delta\theta = 2\Delta u/\text{FOV} = 1.1^\circ$. However, the experiment does not directly address the aliasing caused by the discrete sampling of the detector elements, which may affect the accuracy of the MTF results to some extent.

Another experimental data analysis method presented in this paper is a Gaussian-fitting method in which a Gaussian profile, $\exp[-f^2/(2\sigma^2)]$, was used to fit the measured MTF. How well the Gaussian-fitted profile matches the measured MTF was evaluated. Potentially, this method can simplify the MTF measurement in DPC-CT, as there is only a single fitting parameter σ to be determined. If the MTF of DPC-CT can be experimentally proven to be Gaussian-like, as has been done in ACT (Nickoloff and Riley 1985), its measurement would become simpler and less sensitive to image noise.

4. Experimental results

4.1. Modulation transfer function of absorption CT

The MTFs of the ACT system with different grating setups are shown in figures 7–10. The MTFs with and without the Talbot–Lau interferometer show only a slight difference at high spatial frequencies. The same difference is observed in the MTF measured with only the G0 and G2 gratings, ruling out the diffraction from the G1 grating as the cause. Further, the MTF measured with the modified G0+G2 setup (pre-object, rotated 90° , no phase stepping) shows that the difference in the MTF of ACT is related to neither the periodic structures in the gratings nor x-ray scatter from the gratings ($> 1.5\ \text{m}$ grating-detector distance). Instead, the observed difference is attributed to the use of a finite size cylindrical MTF probe and polychromatic x-rays: beam hardening tends to decrease the value of linear x-ray attenuation coefficient μ near the center of cylindrical objects (shading artifact) due to the relatively large object thickness. As a result, there will be an artifactual increase in the measured MTF of ACT. When the x-ray beam is hardened by the gold-plated gratings, this artifactual enhancement becomes less pronounced, therefore a drop in ACT MTF at medium to high spatial frequency regime will be observed. In other words, the change in the measured MTF does not represent an intrinsic change in the intrinsic spatial resolution of the ACT system. As a parallel demonstration of this

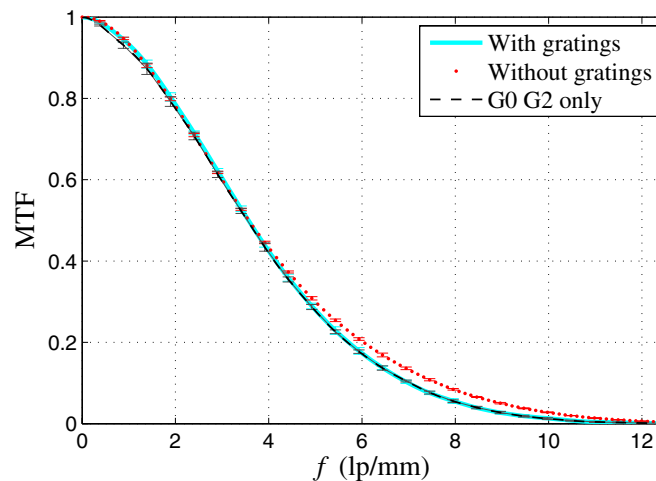


Figure 7. MTF of ACT. The results were measured under three different conditions. (i) All three gratings were used in the system. (ii) None of the gratings were present in the system. (iii) G1 was removed from the system while both G0 and G2 were kept in their designed positions.

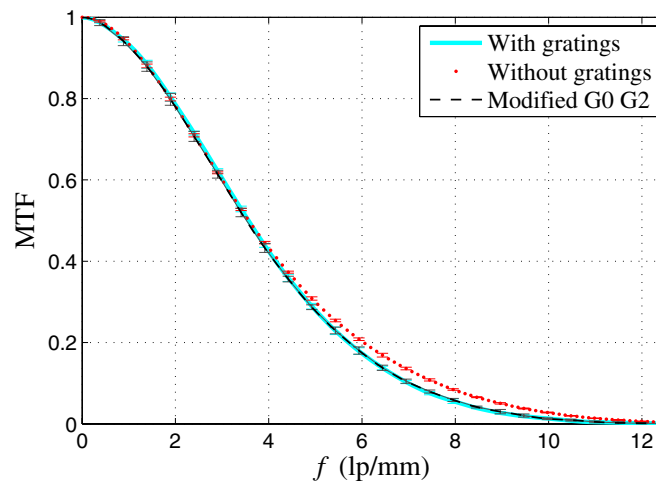


Figure 8. MTF of ACT. The results were measured under three different conditions. (i) All three gratings were used in the system. (ii) None of the gratings were present in the system. (iii) Only the G0 and G2 gratings were placed in the system, and both gratings were rotated 90° about the axis parallel to the x-ray beam, then placed before the object and close to the tube. Phase stepping was performed only in (i).

statement, the presampled detector MTF measured by taking planar projections of a straight edge of a tungsten plate did not change after the interferometer was removed (figure 9).

To further demonstrate the effect of beam hardening on the measured MTF of ACT, all three gratings were removed from the system before a 3.1 mm-thick aluminum plate was attached to the exit window of the x-ray tube to harden the beam. The MTF was still measured using the pencil phantom and the result is shown in figure 10. A similar drop (although not as much since aluminum is much lower in μ compared with gold) in the MTF at high frequencies was observed due to the aluminum filter.

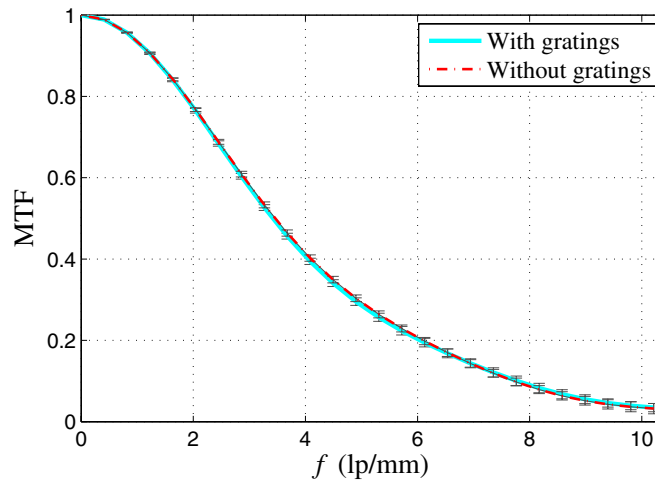


Figure 9. A rectangular tungsten plate with sharp straight edges was used to measure the presampled detector MTF of the our system with and without the gratings in the x-ray beam. The edge was tilted 2.7° relative to the vertical (z) axis. The MTFs with and without gratings were almost identical when measured by the tungsten plate.

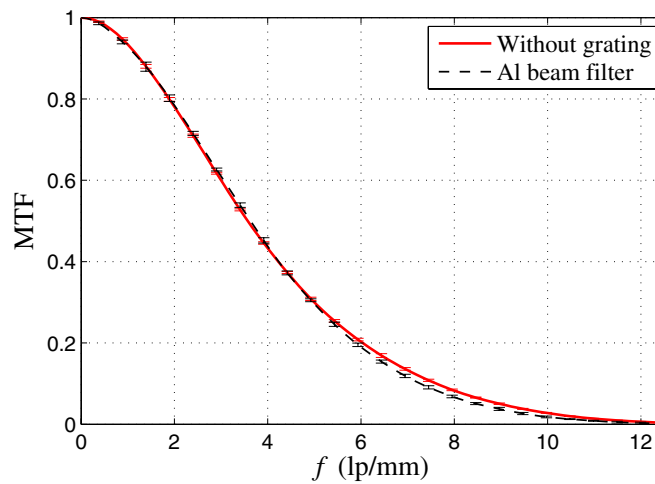


Figure 10. MTF of the ACT system measured without all three gratings (solid line) and with a 3.1-mm-thick aluminum plate attached to the x-ray tube (dashed line).

4.2. Modulation transfer function of differential phase contrast CT

The measured MTF of DPC-CT was plotted and compared with the MTF of ACT in figure 11. Compared with ACT, a noticeable reduction in MTF was observed in DPC-CT. The reduction in MTF is 11% at $f = 2 \text{ lp mm}^{-1}$ and 59% at $f = 6 \text{ lp mm}^{-1}$. The 10% MTFs of ACT and DPC-CT correspond to 7.0 lp mm^{-1} 5.5 lp mm^{-1} respectively in the frequency domain, or $71 \mu\text{m}$ and $91 \mu\text{m}$ respectively in the spatial domain. The difference between the MTFs of DPC-CT and ACT demonstrates the presence of the Talbot–Lau interferometer MTF (T_{TL}).

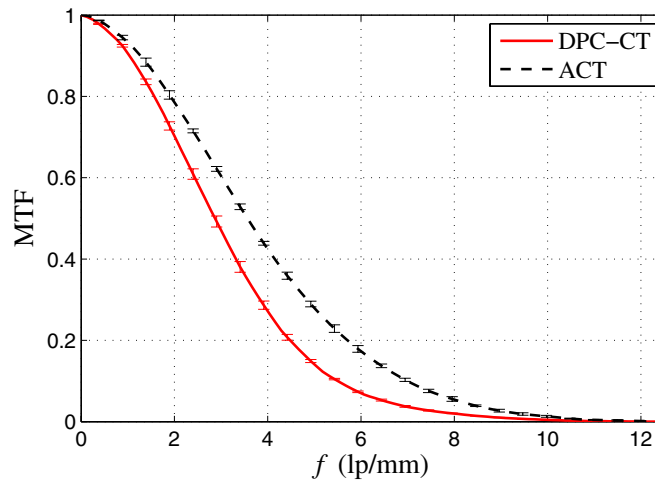


Figure 11. MTFs of DPC-CT (solid line) and the associated ACT with all the gratings present in the beam (dashed line).

Based on (4) and (5), the Talbot–Lau interferometer MTF is given by taking the ratio between the MTFs of DPC-CT and ACT. Based on standard error propagation analysis, the uncertainty of the Talbot–Lau interferometer MTF is given by

$$\begin{aligned}\sigma_{T_{\text{TL}}}^2 &= \left(\frac{\partial T_{\text{TL}}}{\partial \text{MTF}_{\text{dpc}}} \right)^2 \sigma_{\text{MTF}_{\text{dpc}}}^2 + \left(\frac{\partial T_{\text{TL}}}{\partial \text{MTF}_{\text{a}}} \right)^2 \sigma_{\text{MTF}_{\text{a}}}^2 \\ &= \left(\frac{1}{\text{MTF}_{\text{a}}} \right)^2 \sigma_{\text{MTF}_{\text{dpc}}}^2 + \left(-\frac{\text{MTF}_{\text{dpc}}}{\text{MTF}_{\text{a}}^2} \right)^2 \sigma_{\text{MTF}_{\text{a}}}^2.\end{aligned}\quad (9)$$

The measured MTF of the Talbot–Lau interferometer is plotted in figure 12 and is shown only for $f < 9.0 \text{ lp mm}^{-1}$, beyond which the result significantly loses accuracy as the confidence intervals expand dramatically due to the division-by-zero in (9).

4.3. Gaussian-fitting results

The measured MTFs of both DPC-CT and ACT in figure 11 were fitted with Gaussian functions using least-squares minimization and the results were shown in figure 13. Both the DPC-CT and the ACT's MTFs can be approximated as Gaussian functions with decent accuracy (rRMSE = 1.2% for DPC-CT, rRMSE = 1.5% for ACT). The σ values are $= 2.47 \text{ lp mm}^{-1}$ and $= 3.10 \text{ lp mm}^{-1}$ for DPC-CT and ACT, respectively. These results justify the use of the Gaussian model to approximate the MTF of DPC-CT in several earlier works (Li *et al* 2012a, 2012b). Since the Gaussian method is less demanding, it can be used for quick estimations of the MTFs of DPC-CT systems. However, caution should be taken when using this method, as some reconstruction kernels or algorithms may lead to MTFs that are not Gaussian-like (e.g., the lung kernels in Boone 2001).

5. Discussion

The experimental MTF results presented in the previous section validate that the Talbot–Lau interferometer has no influence over the MTF of the ACT system. This is not surprising, since

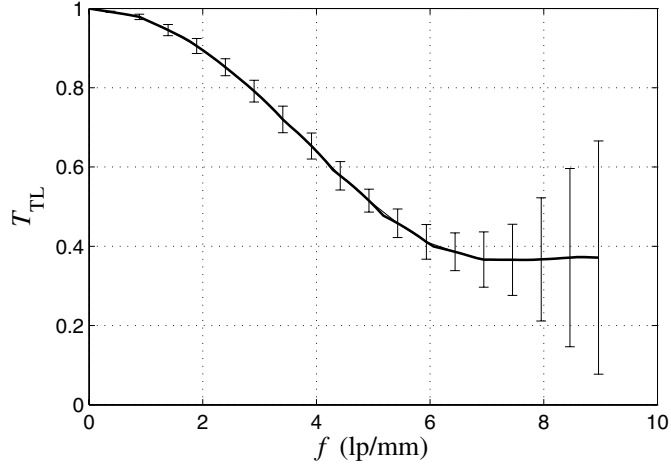


Figure 12. MTF of the Talbot-Lau interferometer (T_{TL}). The error bars represent the 95% confidence interval and were determined from the error bars of the MTFs of ACT and DPC-CT.

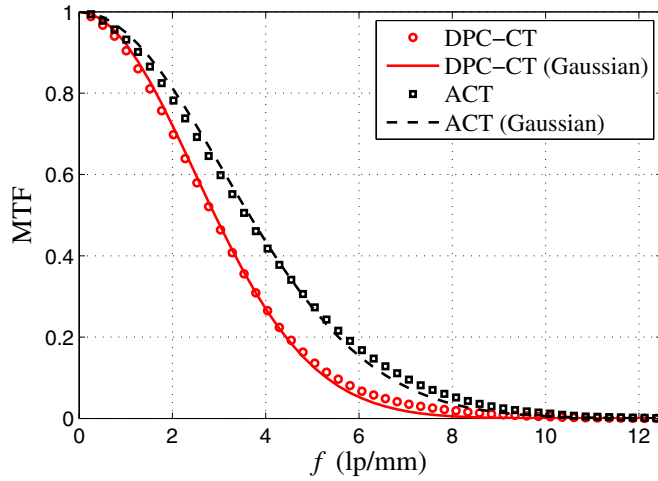


Figure 13. Comparison between the measured MTFs in figure 11 and the Gaussian-fitted MTFs.

the dimensions of the grating structures are too fine to induce any change of the system's spatial resolution. For example, the transmission function of an ideal G0 (with infinitely-thick gold structure) can be expressed in the spatial domain as

$$t_{G0}(u) = \text{rect}\left(\frac{u}{a_0}\right) \otimes \frac{1}{p_0} \sum_{n=-\infty}^{\infty} \delta_{\text{Dirac}}(u - n p_0), \quad (10)$$

where δ_{Dirac} denotes the Dirac delta function, p_0 is the pitch of the G0 grating, a_0 is the width of each opening in G0 (figure 1). In (10), the space between two neighboring gold grating structures is assumed to be a rect function, and the convolution with the comb function

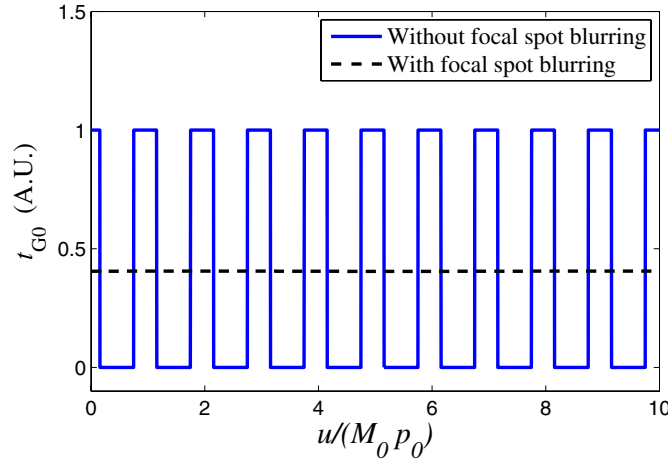


Figure 14. The transmission function of an idealized G0 projected onto the detector axis. The intensity modulation generated by G0 is destroyed by the focal spot blurring.

is performed to replicate the rect function along the u -axis. For systems with a geometric magnification, (10) becomes

$$t_{G0}\left(\frac{u}{M_0}\right) = \text{rect}\left(\frac{u}{M_0 a_0}\right) \otimes \frac{1}{M_0 p_0} \sum_{n=-\infty}^{\infty} \delta_{\text{Dirac}}(u - n M_0 p_0), \quad (11)$$

where M_0 is geometric magnification factor of the G0 grating onto the detector plane. In addition, the transmission function of G0 is subject to geometric blurring from the focal spot given by

$$t'_{G0}\left(\frac{u}{M_0}\right) = t_{G0}\left(\frac{u}{M_0}\right) \otimes t_{\text{spot}}\left[\frac{u}{M_0 - 1}\right], \quad (12)$$

where t_{spot} denotes the transmission function through the x-ray tube focal spot and can be modeled as a Gaussian function with a full width at half maximum of a_{spot} . In a typical setup, the focal spot dimension a_{spot} is larger than p_0 , and therefore the intensity modulation in (11) will be destroyed by the focal spot blur. Figure 14 illustrates an analytical calculation of $t_{G0}(u/M_0)$ and $t'_{G0}(u/M_0)$ of the experimental system used in this paper. M_0 of the system is 8.2 and the nominal value of a_{spot} is 0.1 mm. The transmission function of G0 loses all the intensity modulation at the detector plane due to focal spot blurring. Therefore, the grating structure in G0 is considered to have no influence over the MTF of ACT.

The G2 grating is located after the object, therefore signals from the image object are subject to the finite aperture and discrete sampling of this grating, which can be formulated in the frequency domain as

$$S_{\text{postG2}}(f_u) = S_{\text{preG2}}(f_u) \cdot \text{sinc}(a_2 f_u) \otimes p_2 \sum_k \delta_{\text{Dirac}}\left(f_u - \frac{k}{p_2}\right), \quad (13)$$

where the aperture of G2 is modeled as a rect function with width a_2 (figure 1), S_{preG2} and S_{postG2} are the signals of the object before and after the G2 grating, respectively. In a typical setup, the frequency of G2 ($1/p_2$) is more than ten times larger than the Nyquist frequency determined by pixel size of the system, therefore the influences of both the finite aperture and the sampling of G2 are negligible.

In the simulation work of Köhler *et al* (2011), the ACT setup with gratings sometimes shows a better MTF than the corresponding ACT without gratings. Such an observation was attributed to the edge enhancement induced by coherent illuminations. While perfect spatial coherence can be achieved in simulations, an experimental DPC-CT system using a diagnostic x-ray tube and a source grating, G0, can only produce partially coherent x-rays, making such an edge enhancement insignificant. In addition, perfect temporal coherence (monochromatic x-rays) was assumed in Köhler *et al* (2011); thus, it is not possible to observe the beam hardening-related changes in MTF shown in this paper.

Since all other signal transfer stages in (4) and (5) except T_{TL} were kept the same for the ACT and the DPC-CT systems, the difference in the measured MTFs between the DPC-CT and ACT systems can only be attributed to the use of the Talbot–Lau interferometer, in which a source grating, G0, was used to split the polychromatic beam into many partially coherent (with respect to spatial coherence) beamlets. Note that in theory it has been assumed that the interference patterns from each beamlet will be perfectly aligned with one another to maximize the use of available photons generated from the x-ray tube. However, this perfect alignment of interference patterns can only be formed for monochromatic x-ray beams with perfect coherence. If a polychromatic x-ray beam with partial coherence were used, the sharpness of the combined interference pattern from all beamlets would be degraded, and thus an effective blur of the image object was generated. This effective blur is responsible for the observed degradation of MTF in this paper. Note that, in numerical simulation studies published to date, monochromaticity and perfectly spatially coherent x-rays (no G0) were used (Köhler *et al* 2011, Raupach and Flohr 2011, Tang *et al* 2012). Such a difference in system condition between numerical simulations and our experimental system explains why the degradation in the MTF of DPC-CT was not observed in numerical simulations. In the future, it would be interesting and highly desirable to include the effect of G0 grating in the numerical models to quantify how exactly the presence of G0 grating leads to the observed degradation in MTF reported in this work.

Strictly speaking, an accurate MTF measurement requires all data involved to be free of aliasing. The experimental design of this work reflects efforts to minimize aliasing. However, the intrinsic aliasing due to the detector sampling still exists in the presented data, which may affect the quantitatively accuracy of the MTF results (particularly at high spatial frequencies). In ACT, the presampled MTF can be measured using methods such as the one developed by Boone (2001), in which an angled thin aluminum foil was used to increase the effective sampling rate. Unfortunately, this method is not directly applicable to DPC-CT for the reasons stated in section 3.1.

6. Conclusions

In conclusion, the spatial resolution of an experimental differential phase contrast-computed tomography (DPC-CT) system and the associated absorption CT system were quantitatively characterized via modulation transfer function (MTF) measurements. A new experimental method using an inexpensive and readily available phantom (a mechanical pencil refill) was developed to address several practical challenges in measuring the MTF of DPC-CT. The results of this work show that the Talbot–Lau interferometer does not influence the intrinsic spatial resolution of the absorption CT system, but it does lead to a slight degradation in the MTF of the DPC-CT system when compared with that of the associated absorption CT system. The per cent reduction in MTF is 11% at 2 lp mm⁻¹ but increases to 59% at 6 lp mm⁻¹. Based upon the experimental results from this paper and numerical simulations by others, the degradation of MTF in DPC-CT is attributed to the presence of the source grating G0.

Further theoretical modeling of DPC-CT systems that includes the source grating G0 would be needed to ultimately pinpoint the exact transfer process of DPC signals through the entire interferometer with the three gratings.

Acknowledgments

The authors would like to thank Dr Walter Pepler and Dr Frank Ranallo for discussions on the MTF measurements in x-ray absorption imaging. The authors would also like to thank John Garrett for his editorial assistance.

References

- Beutel J, Kundel H and Van Metter R (ed) 2000 *Handbook of Medical Imaging (Physics and Psychophysics vol 1)* (Bellingham, WA: SPIE Press)
- Bevins N, Zambelli J, Li K, Qi Z and Chen G-H 2012 Multicontrast x-ray computed tomography imaging using Talbot-Lau interferometry without phase stepping *Med. Phys.* **39** 424–8
- Bischof C J and Ehrhardt J C 1977 Modulation transfer function of the EMI CT head scanner *Med. Phys.* **4** 163–7
- Boone J M 2001 Determination of the presampled MTF in computed tomography *Med. Phys.* **28** 356–60
- Chen G-H, Zambelli J, Li K, Bevins N and Qi Z 2011 Scaling law for noise variance and spatial resolution in differential phase contrast computed tomography *Med. Phys.* **38** 584–8
- David C, Nohammer B, Solak H H and Ziegler E 2002 Differential x-ray phase contrast imaging using a shearing interferometer *Appl. Phys. Lett.* **81** 3287–9
- Dobbins J T, Ergun D L, Rutz L, Hinshaw D A, Blume H and Clark D C 1995 DQE (f) of four generations of computed radiography acquisition devices *Med. Phys.* **22** 1581–93
- Fujita H, Tsai D, Itoh T, Doi K, Morishita J, Ueda K and Ohtsuka A 1992 A simple method for determining the modulation transfer function in digital radiography *IEEE Trans. Med. Imaging* **11** 34–9
- Huang Z, Kang K, Li Z, Zhu P, Yuan Q, Huang W, Wang J and Yu A 2006 Direct computed tomographic reconstruction for directional-derivative projections of computed tomography of diffraction enhanced imaging *Appl. Phys. Lett.* **89** 041124
- Kitchen M, Paganin D, Uesugi K, Allison B, Lewis R, Hooper S and Pavlov K 2011 Phase contrast image segmentation using a Laue analyser crystal *Phys. Med. Biol.* **56** 515–34
- Köhler T, Engel K J and Roessler E 2011 Noise properties of grating-based x-ray phase contrast computed tomography *Med. Phys.* **38** S106–16
- Kottler C, Revol V, Kaufmann R and Urban C 2010 Dual energy phase contrast x-ray imaging with Talbot-Lau interferometer *J. Appl. Phys.* **108** 114906
- Li K, Bevins N, Zambelli J and Chen G-H 2012a A new image reconstruction method to improve noise properties in x-ray differential phase contrast computed tomography *Proc. SPIE* **8313** 83131V
- Li K, Bevins N, Zambelli J and Chen G-H 2013 Fundamental relationship between the noise properties of grating-based differential phase contrast CT and absorption CT: theoretical framework using a cascaded system model and experimental validation *Med. Phys.* **40** 021908
- Li K, Bevins N, Zambelli J, Qi Z and Chen G-H 2012b Detection performance study for cone-beam differential phase contrast CT *Proc. SPIE* **8313** 83131L
- Momose A, Kawamoto S, Koyama I, Hamaishi Y, Takai H and Suzuki Y 2003 Demonstration of x-ray Talbot interferometry *Japan. J. Appl. Phys.* **42** 866–8
- Nickoloff E and Riley R 1985 A simplified approach for modulation transfer function determinations in computed tomography *Med. Phys.* **12** 437–42
- Olivo A and Speller R 2008 Image formation principles in coded-aperture based x-ray phase contrast imaging *Phys. Med. Biol.* **53** 6461–74
- Pfeiffer F, Bech M, Bunk O, Kraft P, Eikenberry E F, Brönnimann C, Grünzweig C and David C 2008 Hard-x-ray dark-field imaging using a grating interferometer *Nature Mater.* **7** 134–7
- Pfeiffer F, Kottler C, Bunk O and David C 2007 Hard x-ray phase tomography with low-brilliance sources *Phys. Rev. Lett.* **98** 108105
- Pfeiffer F, Weitkamp T, Bunk O and David C 2006 Phase retrieval and differential phase-contrast imaging with low-brilliance x-ray sources *Nature Phys.* **2** 258–61
- Qi Z and Chen G-H 2008 Direct fan-beam reconstruction algorithm via filtered backprojection for differential phase-contrast computed tomography *X-Ray Opt. Instrum.* **2008** 835172

- Qi Z, Zambelli J, Bevins N and Chen G-H 2010 Quantitative imaging of electron density and effective atomic number using phase contrast CT *Phys. Med. Biol.* **55** 2669–77
- Raupach R and Flohr T 2011 Analytical evaluation of the signal and noise propagation in x-ray differential phase-contrast computed tomography *Phys. Med. Biol.* **56** 2219–44
- Richard S, Husarik D, Yadava G and Samei E 2012 Towards task-based assessment of CT performance: system and object MTF across different reconstruction algorithms *Med. Phys.* **39** 4115–22
- Tang X, Yang Y and Tang S 2011 Characterization of imaging performance in differential phase contrast CT compared with the conventional CT-noise power spectrum NPS(k) *Med. Phys.* **38** 4386–95
- Tang X, Yang Y and Tang S 2012 Characterization of imaging performance in differential phase contrast CT compared with the conventional CT: spectrum of noise equivalent quanta NEQ(k) *Med. Phys.* **39** 4467–82
- Tward D and Siewerdsen J 2008 Cascaded systems analysis of the 3D noise transfer characteristics of flat-panel cone-beam CT *Med. Phys.* **35** 5510–29
- Wen H, Bennett E, Hegedus M and Carroll S 2008 Spatial harmonic imaging of x-ray scattering-initial results *IEEE Trans. Med. Imaging* **27** 997–1002
- Zambelli J, Bevins N, Qi Z and Chen G-H 2010 Radiation dose efficiency comparison between differential phase contrast CT and conventional absorption CT *Med. Phys.* **37** 2473–9
- Zambelli J, Li K, Bevins N, Qi Z and Chen G-H 2011 Noise characteristics of x-ray differential phase contrast CT *Proc. SPIE* **7961** 79613N